Reviews of Electromagnetics, Vol. IV, 2025
EuCAP 2025 Special Issue
DOI: 10.53792/RoE/2025/25019

Reviews of Electromagnetics
EuCAP 2025 Special Issue

Beam-Steered Channel Measurements at 160 GHz in an Industrial Environment

Alper Schultze[1]*, Mathis Schmieder[1], Ramez Askar[1], Michael Peter[1], Wilhelm Keusgen[2], Taro Eichler[3]

Abstract
This work presents further results of a channel measurement campaign carried out in a production hall of Rohde & Schwarz in Memmingen, Germany. The channel measurements were performed in the D-Band at a carrier frequency of 160 GHz with a time domain correlation based channel sounder. The beam-steered channel measurements were analyzed and evaluated on the basis of identified beam pair realizations regarding MIMO capabilities, macro-diversity gains and blockage effects for a multi-transmitter industrial sub-terahertz communication system.

Key terms
channel sounding; sub-terahertz; beam-steering; macro-diversity; blockage

[1] *Fraunhofer Institute for Telecommunications, Heinrich Hertz Institute, HHI, Berlin, Germany*
[2] *Department of High Frequency Systems, Technische Universität Berlin, Germany*
[3] *Rohde & Schwarz, Munich, Germany*
***Corresponding author**: alper.schultze@hhi.fraunhofer.de

Received: 24/05/2025, Accepted: 30/08/2025, Published: 28/11/2025

1. Introduction

Future generations of mobile communication standards envision an expansion of the frequency spectrum to sub-terahertz (sub-THz) bands to meet the ever increasing demand for high data rates. To be more specific: The frequency range between 100 GHz and 3 THz is regulated by the International Telecommunication Union (ITU) ITU-R Radio Regulations [1]. Between 100 GHz to 275 GHz, 8 frequency bands with sufficient contiguous bandwidths are allocated to fixed and mobile service, constituting 90.7 GHz bandwidth in total. Four of these bands are located within the sub-THz D-band (110 GHz to 170 GHz) range. One of these bands is a band ranging from 151.5 GHz to 164 GHz, which is the frequency band of interest for this paper.

Besides the ITU, the terahertz (THz) Industry Specification Group (ISG) from the European Telecommunications Standards Institute (ETSI) has released its first four group reports with recommendations on use cases, frequency bands, channel modeling and radio frequency (RF) hardware for THz technologies [2, 3, 4, 5]. The first group report [2] identifies 19 use cases such as real-time industrial control. The second group report [3] identifies 8 frequency bands in the frequency range from 100 GHz to 275 GHz GHz such as Frequency Band 3: 151.5 GHz to 164 GHz.

As a result, THz communication has become an area of growing interest in the scientific community in recent years due to the promise of large unused bandwidths. Prior to the standardization of mobile communication standards, channel measurements have to be performed in different environments to observe the behavior of the radio channel. Therefore, we present a study for propagation at 160 GHz in an indoor factory environment.

A few recent articles have presented results of industrial channel measurements in sub-THz bands, specifically in the D-band (110 GHz to 170 GHz and H-band (220 GHz to 325 GHz). In the H-band, with the exception of [13] that reported channel measurements at a center frequency (CF) of 220 GHz, the rest of the published articles reported measurements around a CF of 300 ± 6 GHz [10, 14, 15, 16, 17]. However, state-of-the-art reported four carrier frequencies in the D-band: In [6], the CF was 132 GHz, in [7, 8, 9], the CF was 142 GHz and in [10], the CF was 145 GHz. Moreover, former works of this paper group [11, 12] used a CF of 160 GHz, as in this work. Table 1 summarizes the main parameters of these state-of-the-art sub-THz industrial channel measurements.

In [12] first evaluations of a beam-steered sub-terahertz (sub-THz) channel measurement campaign in D-band have been

Table 1: Sub-THz (D-Band & H-Band) State-of-the-Art Channel Measurements in Industrial Environments

Work	Team	Carrier frequency	Bandwidth	Channel sounder type
D-band (110 GHz to 170 GHz)				
[6]	Chongqing	132 GHz	5.5 GHz	VNA[a]
[7, 8, 9]	NYU	142 GHz	4 GHz	TD[b] Sliding correlation
[10]	Durham	145 GHz	2 GHz	FMCW[c]
[11, 12] **and this**	FhG-HHI	160 GHz	2 GHz	TD[b] FZC[d] sequence
H-band (220 GHz to 330 GHz)				
[13]	Chongqing	220 GHz	10 GHz	VNA[a]
[10]	Durham	294 GHz	2 GHz	FMCW[c]
[14, 15]	FhG-HHI	300 GHz	2 GHz	TD[b] FZC[d] sequence
[16]	TUIL	303.8 GHz	5 GHz	TD[b] 12bit m-sequence
[15, 17]	TUBS	304.2 GHz	8 GHz	TD[b] m-sequence

[a] Vector Network Analyzer
[b] Time-domain
[c] Frequency Modulated Continuous Waveform
[d] Frank Zadoff Chu

presented and essential parameters such as normalized received power (NRP), total normalized received power (TNRP) and macro-diversity gain (MDG) have been introduced. In comparison to [12], this work extends the evaluation of the beam-steered sub-THz channel measurements by expanding the investigations of the NRP for one and multiple beam pair realizations (BPRs). This expansion now covers an optimistic and realistic adoption of an industrial sub-THz communication system. This differentiation is also applied for the MDG investigation. Additionally, a joint evaluation of all possible BPRs for one measurement position is introduced and its robustness against blockage effects is evaluated. By comparing three blockage scenarios (no blockage, single-directional blockage and multi-directional blockage), the expected NRP is evaluated. The blockage is synthetically applied in postprocessing.

To the best of the author's knowledge this is the first scientific publication that evaluates channel measurements in the D-band with regards to beam-steering, multiple-input multiple-output (MIMO) and MDGs.

The rest of the paper is organized as follows: Section 2 introduces the channel sounder setup, describes its components and the operating principle. Section 3 introduces the indoor factory that served as venue for the channel measurements and the procedure of the channel measurement campaign. Section 4 will introduce the measurement data evaluation algorithm and its results. Finally, Section 5 concludes the paper and gives an outlook on future work.

2. Channel Sounder Setup

The setup used for carrying out the sub-THz channel measurements is a time domain correlation (TDC) based channel sounder (CS) [18]. All CS realizations like TDC based, vector network analyzer (VNA) based and time domain spectroscopy (TDS) have their unique features, advantages and disadvantages. Depending on the availability and measurement campaign, a suitable CS has to be chosen. In comparison to other CS realizations such as TDS or VNA based, the TDC principle allows large and true untethered spatial separation between transmitter (TX) and receiver (RX). Although radio over fiber (RoF) expansion techniques for VNA based CSs enable long-range measurements for up to several hundreds of meters at sub-THz frequencies [19, 20], the developed TDC based CS supports true untethered separation of the TX and RX by utilizing two synchronized reference clocks when needed. This allows the characterization of large environments such as production halls [21].

The developed CS operates in the D-band (110 GHz to 170 GHz) with a targeted frequency range of 159 GHz to 161 GHz, which leads to a CF of 160 GHz and a measurement bandwidth of 2 GHz. It is realized with state-of-the-art measurement and test equipment by Rohde & Schwarz and the Fraunhofer society. Fig. 1 visualizes the block diagram of the D-band TDC based CS setup that was used. The following paragraphs will give a detailed description of the setup's components and the setup's operating principle.

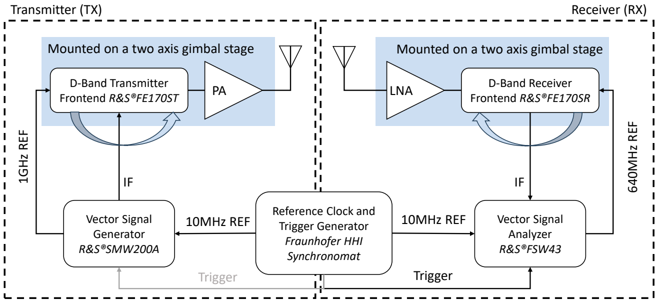

Figure 1: Block diagram of the CS setup, visualizing its components and connections.

The core components of the sub-THz CS are a vector signal generator (VSG) (R&S®SMW200A), an up-converting D-band front end (FE) (R&S®FE170ST), a vector signal analyzer (VSA) (R&S®FSW43), a down-converting D-band FE (R&S®FE170SR) and a reference clock and trigger generator (Fraunhofer HHI Synchronomat). The VSG and the up-converting D-band FE form the TX of the setup, the VSA and the down-converting D-band FE form the RX of the setup, and the reference clock and trigger generator forms the setup's time source [22]. As TX antenna system [23], a custom waveguide sector horn antenna and an RF domain power amplifier (PA) (Fraunhofer IAF M286AMPG) are used. The custom waveguide sector horn antenna has an approx. gain of 20 dBi, a half-power beam width (HPBW) of 15° in E-plane and a HPBW of 55° in H-plane. The PA (Fraunhofer IAF M286AMPG) has a gain of 21 dB at 160 GHz and a 1-dB compression piont (P1dB) of 10 dBm. As RX antenna system, a commercial-off-the-shelf (COTS) waveguide probe antenna (Eravant SAP-06-R2) and a COTS D-band low noise amplifier (LNA) (AT Microwave AT-LNA-110170-3306E) are used. The probe antenna (Eravant SAP-06-R2) has a typical gain of 6.5 dBi, a HPBW of 115° in E-plane and a HPBW of 60° in H-plane. The LNA (AT Microwave AT-LNA-110170-3306E) has a gain of 33 dB at 160 GHz and a P1dB of −3 dBm. Both antenna systems are mounted co-polarized vertically in the E-plane. To enable angle-resolved measurements both at the TX and RX side, the two FEs are mounted each on a two axis gimbal stage (Zaber X-G-RST-DE) that allows tilts from 0° to 360° both in the azimuth and elevation domain. In contrast to a prior work [11] where the FEs were tilted in the elevation domain, in this work the FEs are only tilted in the azimuth domain. Fig. 2 and Fig. 3 show a close up photograph each of the RX and the TX, depicting the sub-THz FEs with PA, LNA and antennas mounted on the two axis gimbal stages.

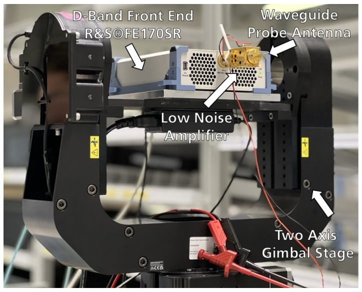

Figure 2: RX

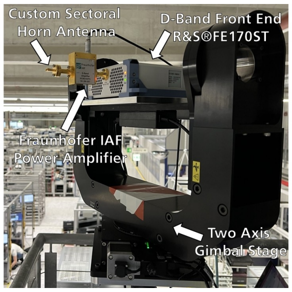

Figure 3: TX

The basic operating principle of the introduced sub-THz D-band CS is as follows: The VSG acts as a continuous stimulus generator and provides the apriori known complex broadband sounding sequence at an intermediate frequency (IF) for the up-converting D-band TX FE. As sounding sequence, a 200 kSample long Frank-Zadoff-Chu (FZC) sequence is used [24]. With the mentioned measurement bandwidth of 2 GHz, which is the maximum the VSG can provide, the sequence duration is 100 µs. FZC sequences are complex-valued chirp sequence that have perfect correlation properties and are therefore ideally suited for channel sounding. After an initial trigger, the sounding sequence is generated continuously repeated. The generated trigger is coherent to the 10 MHz reference output of the reference clock and trigger generator. The D-band TX FE does an up-conversion of the sounding sequence to the mentioned CF of 160 GHz and also transmits it continuously repeated. For the up-conversion, the FE generates its own internal local oscillator (LO) that is locked to a 1 GHz reference signal provided by the VSG, for coherent transmission. The output of the FE is afterwards amplified in the RF domain by the PA. To overcome high path losses (PLs), a directive high gain antenna is used. To cover a large area by the TX in the azimuth domain, the TX FE is rotated with the help of a two-axis gimbal stage from −60° to 60° in 15° steps.

The transmitted signal, that has undergone the influence of the wireless channel is received by the RX antenna, amplified by the LNA and afterwards down-converted to an IF by the RX FE. Similar as to the TX FE, the RX FE generates its own internal LO that is locked to a 640 MHz reference signal provided by the VSA. The down-converted signal is provided to the VSA which starts coherently sampling the signal after triggered. The VSA can sample an arbitrary number of sounding sequences, until its sample storage is full. For this work, the number of sounding sequences recorded per measurement, also denoted as the number of snapshots, is 250. The recorded snapshots are afterwards stored on the internal storage of the VSA.

Both the VSG and the VSA use the 10 MHz reference output of the Fraunhofer HHI Synchronomat, which is a high precision rubidium clock and trigger generator. This device enables coherent triggering and coherent sampling of the transmitted sounding sequences. Therefore, the CS setup has a true time reference for the TX and RX.

Table 2 summarizes in its first part the core CS parameters regarding frequency, sounding sequence, antennas and amplifiers.

Table 2: Channel Sounder Setup Parameters

Parameter	Value and unit
Center frequency	160 GHz
Measurement bandwidth	2 GHz
Frequency range	159 GHz to 161 GHz
Sequence type	FZC [24]
Sequence length	200 kSample
Sequence duration	100 µs
Number of snapshots	250
TX antenna gain	20 dBi
TX antenna HPBW in E-plane	15°
TX antenna HPBW in H-plane	55°
RX antenna gain	6.5 dBi
RX antenna HPBW E-plane	115°
RX antenna HPBW H-plane	60°
Gain of PA at TX-side	21 dB
Gain of LNA at RX-side	33 dB
Antenna polarization	Vertical-Vertical (E-plane)
AAoD range	−60° to 60°
AAoD resolution	15°
Number of AAoD angles	9
AAoA range	0° to 270°
AAoA resolution	90°
Number of AAoA angles	4
Correlation gain	53.0 dB
Averaging gain	24.0 dB
Processing gain	77.0 dB
Dynamic range	> 60 dB
Relative noise floor	≈ -140 dB

Regarding the CS setup's error resilience and possible measurement inaccuracies the following things play a great role: amplitude error, phase stability and angle alignment inaccuracies. In [25], the effects and consequences of amplitude error and phase stability are discussed. The amplitude error may result from improper calibration of the CS setup or nonlinearities of its components. Thermal noise, phase noise and timing jitter may result in inaccuracies. Phase instabilities affect the accuracy of angle estimation algorithms and coherent averaging. Since this work does not include angular estimation, it will not be discussed further. Coherent averaging aims for an improvement of the CS's dynamic range in postprocessing. The basic conditions for an improvement of the dynamic range are a static channel and a stable phase. Angle alignment inaccuracies are caused by the operators when moving the RX between measurement position, the setup of the CS, as well as imprecisions of the two-axis-gimbals. The gimbals are high precision motion control components with a high reproducibility of tilt angles so their inaccuracies are negligible. Angle alignment errors distort the granularity of the beam-steering and may result in inaccuracies in postprocessing. During measurement campaign execution, errors caused by the operators have been tried to keep at a minimum.

3. Measurement Scenario and Procedure

The sub-THz channel measurements were conducted in a production hall of Rohde & Schwarz in Memmingen, Germany. Measurement instruments are manufactured, assembled and tested over an area of 70 m x 100 m in the industrial factory. The production hall is throughout densely packed with metal objects such as shelves and test benches, as typical for an industrial surrounding. Further metal objects such as corrugated plates and air tubes are located at the production hall's ceiling. Both the ceiling and the walls are made of concrete and the floor is made of anti-static flooring. Along two sides of the production hall - south and west - there is a continuous balcony at a height of 3.2 m. Fig. 4 shows a photo of the production hall taken from the balcony depicting the measurement environment's composition.

Figure 4: Photograph of the measurement environment taken from the balcony depicting the measurement environment's composition.

On the aforementioned balcony the TX was placed at two positions: one position at the west side and one position at the south side of the balcony. The resulting TX antenna height was at 5 m above the ground for both positions (3.2 m height of balcony + 1.8 m TX antenna height). The TX positions were chosen as such that the TX is covering two major aisles of the production hall. One aisle is a west-to-east connection and the other one a north-to-south connection of the production hall. Bseides the mentioned aisles, other corridors of the production hall also served as orientation for the RX placement. The RX was placed at 6 positions in the production hall: 5 positions in corridors and one position in the production area between test benches. The RX was placed at a height of 1.75 m above ground. Overall, TX-RX distances (3D) of 17.24 m to 50.81 m are covered in the measurement scenario. Table 3 summarizes the measurement scenario parameters.

Table 3: Measurement Scenario Parameters

Parameter	Value and unit
Venue	Production hall
Environment	Industrial
Floor area	70 m x 100 m
Number of TX positions	2
Number of RX positions	6
Total number of measurements	12
Number of LOS positions	7
Number of NLOS positions	5
TX antenna height	5.00 m
RX antenna height	1.75 m
TX-RX distance (3D)	17.24 m to 50.81 m

Fig. 5 illustrates the floor plan of the production hall. The light gray shaded areas on the left (west) and bottom side (south) of the figure illustrate the continuous balcony on which the TX was placed. The two red crosses symbolize the TX positions - position 1 on the left and position 2 on the bottom side of the illustration. The six green crosses symbolize the RX positions (MP9, MP25, MP34, MP50, MP80, MP115). For the sake of consistency for future publications, the indexing of the RX positions is not changed. The red and the green arrows symbolize the 0° orientation of the TX and RX, respectively.

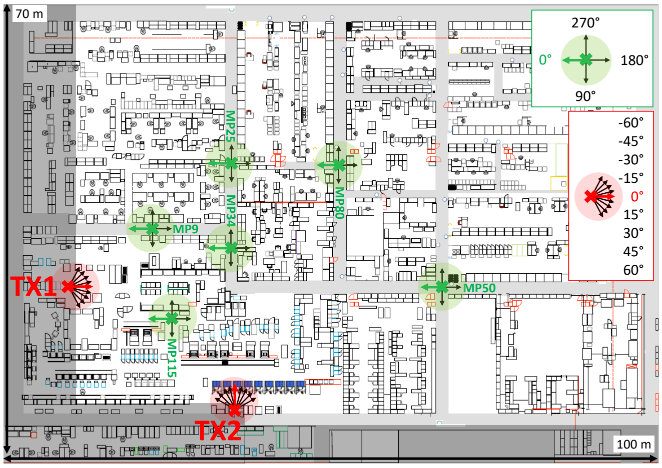

Figure 5: Floor plan of the production hall with marked TX positions as red crosses and RX positions marked as green crosses. The red and green arrows signal the 0° orientation of the TX and RX respectively. On the right side, a legend for all other angles is provided.

The measurement campaign targeted beam-steered channel measurement, therefore the TX and RX were rotated both in the azimuth plane. The TX was rotated from –60° to 60° in 15° steps which resulted in 9 angles (–60°, –45°, –30°, –15°, 0°, 15°, 30°, 45°, 60°). The RX was rotated from 0° to 270° in 90° steps which resulted in 4 angles (0°, 90°, 180°, 270°). The azimuth angle of departure (AAoD) and azimuth angle of arrival (AAoA) resolution/step size resulted from the HPBW of the used antennas mentioned in the previous section (Sec. 2). Table 2 summarizes the AAoD and AAoA parameters in its second part.

For each measurement position, all AAoD and all AAoA combinations were measured which resulted in 36 measurements per measurement position. In addition, for both TX positions all RX positions were measured which resulted in a total of 12 measurement positions, each consisting of 36 measurements. Each measurement was therefore defined in TX position, RX position, AAoD and AAoA.

Regarding line-of-sight (LOS) and non-line-of-sight (NLOS) conditions, the selected measurement positions covered all possible combinations. This means that for certain RX positions a LOS for both TX positions was present (MP9 and MP34). The same applies for the NLOS condition (MP80). Additionally, for certain RX positions either TX position 1 or TX position 2 had a LOS and the other a NLOS (MP25, MP50, MP115). Table 4 gives an overview of the measurement positions, listing the RX position, TX position and the LOS or NLOS condition.

Table 4: Overview of Measurement Positions

Index	RX pos.	TX pos.	LOS/ NLOS
1	9	1	LOS
2	9	2	LOS
3	25	1	NLOS
4	25	2	LOS
5	34	1	LOS
6	34	2	LOS
7	50	1	LOS
8	50	2	NLOS
9	80	1	NLOS
10	80	2	NLOS
11	115	1	NLOS
12	115	2	LOS

4. Measurement Evaluation

The captured measurement data (baseband (BB) inphase- and quadrature- (I-/Q-)samples) are processed offline after the measurement campaign's execution in Matlab. The evaluation algorithm consists of multiple consecutive processing steps that include a phase correction of the common phase error, the convolution with a back-to-back (B2B) calibration that was recorded right before the measurement campaign's execution, a windowing in the time domain (TD) with a Kaiser-Bessel window and a coherent averaging of the obtained channel responses over the number of snapshots, to finally obtain an average channel impulse response (ACIR) for each measurement. By using a sequence length of 200 kSample the correlation gain is 53.0 dB. The averaging gain results from the number of snapshots and is 24.0 dB. Correlation and averaging gain summed up described the processing gain of the system and is 77.0 dB.

Fig. 6 and Fig. 7 show two exemplary ACIRs for RX position 34, one for TX position 1 and the other for TX position 2. As listed in Table 4, RX position 34 is a LOS case for both TX positions. The ACIRs are plotted as magnitude in dB over delay in ns. The magnitude is normalized to the B2B calibration and incorporates the TX antenna gain, the RX antenna gain and the PL. Thanks to the CS setup's coherence, the delay represents the electromagnetic wave's exact time of travel. In addition to the ACIRs, the ACIRs' individual 0.99-quantile is visualized as a red dashed line. The 0.99-quantile represents the CS's noise floor [26]. To be sure, that for all following processing steps no noise sample is regarded, an evaluation threshold is applied that is 10 dB above the 0.99-quantile. The evaluation threshold is visualized as green dashed line. Both shown ACIRs are the result of the best beam pair measurement for RX position 34 and TX position 1 and 2, respectively (measurement index 5 and 6). Fig. 6 shows the ACIR of the measurement taken at RX position 34, with the TX located at position 1 aligned to an AAoD of −15° and the RX aligned to an AAoA of 0°. Fig. 7 shows the ACIR of the measurement taken also at RX position 34 but the TX located at position 2, with the TX aligned to an AAoD of 0° and the RX aligned to an AAoA of 90°. The figure also provides an enlarged view (zoom) to the strongest path.

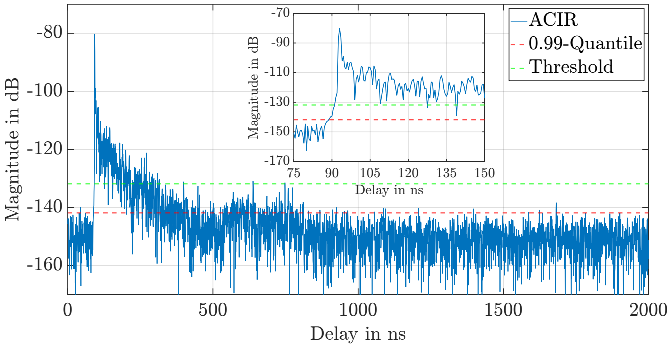

Figure 6: ACIR for the best BPR of measurement index 5: RX position 34, TX position 1, 0° AAoA and −15° AAoD. Source: [12]

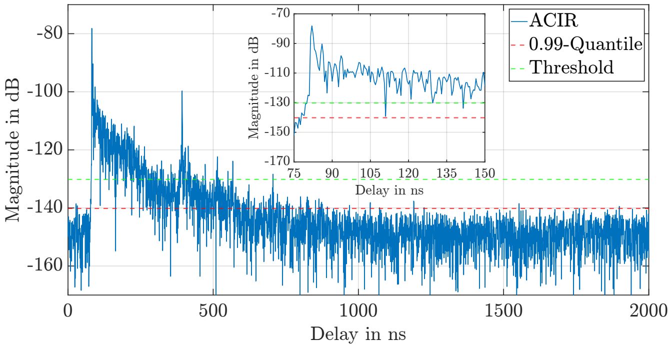

Figure 7: ACIR for the best BPR of measurement index 6: RX position 34, TX position 2, 90° AAoA and 0° AAoD. Source: [12]

Fig. 6 and Fig. 7 report that for both ACIRs the most dominant path belongs to the LOS path, as expected. Since measurement position MP34 has a similar distance from TX position 1 to the RX as from TX position 2 to the RX, the delay and magnitude of the LOS path are similar for both ACIRs. Close by the LOS path, one to two additional paths that are roughly

20 dB below the LOS path are observable. In contrast to Fig. 6, Fig. 7 reports a strong (20 dB below LOS path) late arriving path. The average 0.99-quantile which represents the CS's noise floor lies around −140 dB for both ACIRs. This verifies that the CS has an exceptionally high dynamic range of over 60 dB. Table 2 summarizes the parameters regarding evaluation gains, dynamic range and relative noise floor in its third part.

Fig. 6 and Fig. 7 represent the best BPR for RX position 34 and TX position 1 and 2, respectively. From a sub-THz communication system point of view, the best BPR corresponds to the TX-RX configuration which allows the highest received power to be achieved. The TX-RX configuration includes the antenna characteristics and also the angular dependent beam-steering setting.

Expanding the view from the best BPR for a measurement to the whole angular representation, all 36 measurements have to be regarded. One option of visualizing all BPRs for one TX-RX configuration is the power angular profile (PAP). To obtain the PAP, for each of the 36 ACIRs the magnitudes above the evaluation threshold are summed up. The summed up magnitudes represent the NRP in dB for one BPR. Fig. 8 and Fig. 9 visualize two exemplary PAPs for measurement index 5 (Fig. 8) and measurement index 6 (Fig. 9), completing Fig. 6 and Fig. 7 with the residual BPRs. The PAPs are displayed as pixels with scaled colors, where the y-axis represents the AAoA and the x-axis represents the AAoD. The color of each pixel represents the NRP in dB for a specific BPR.

From a sub-THz communication system point of view, the PAP covers all possible TX-RX configuration with the setup used. This includes the properties of the antennas used and also the granularity of the angular steering. The PAPs report a strong angular dependence of the NRPs of the BPRs. This means that neighboring BPRs affect each other due to scattering and reflections caused by the industrial environment. To decrease the complexity of the system, independent BPRs are to be identified.

Independent BPRs are identified by finding local maxima of the PAP. The identified local maxima of the PAP are highlighted as red frames around certain pixels in Fig. 8 and Fig. 9. The global maximum (local maxima with the highest NRP) corresponds to the best BPR and is highlighted with a red cross.

Fig. 8 reports that the best BPR for measurement index 5 is 0° AAoA and −15° AAoD with a NRP of −73.1 dB. Fig. 9 reports that the best BPR for measurement index 6 is 90° AAoA and 0° AAoD with a NRP of −68.3 dB. Besides the best BPR, two to three additional BPRs (local maxima) are identified for measurement index 5 and 6 respectively. In comparison to other measurements, up to 5 BPRs are detected. For both PAPs the majority of other identified local maxima are shifted 180° in AAoA. This implies: In LOS cases, usable BPRs, other than the best BPR, are mainly located at the opposite side of the LOS path and may be products of the LOS path's reflections.

The measurements report that in over 90 % of cases, the second strongest BPR is shifted by 180° from the strongest/best BPR. This finding is valid for both LOS and NLOS measurement positions and implies, that the composition of the industrial measurement environment causes these multipath components (MPCs).

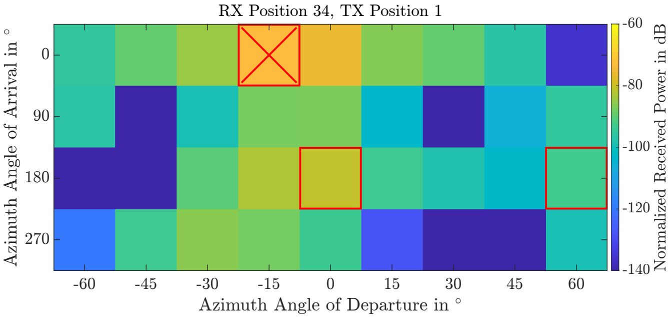

Figure 8: PAP for measurement index 5: RX position 34, TX position 1. Source: [12]

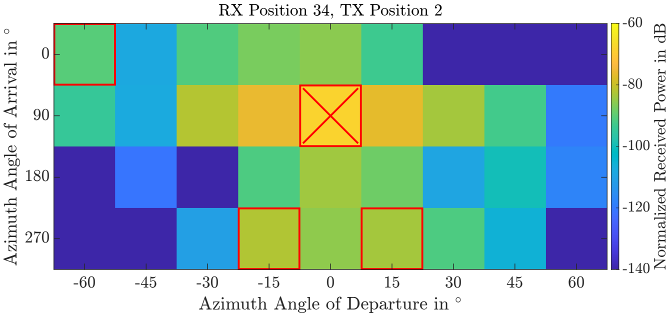

Figure 9: PAP for measurement index 6: RX position 34, TX position 2. Source: [12]

To address the topic of MIMO capability of a potential sub-THz communication system, the TNRP of each of the 12 measurements is analyzed. Therefore, all identified local maxima - all BPRs - of a PAP are summed up. The results are 12 scalar values, each representing a measurement and therefore a specific TX-RX configuration. The TNRP represents received power at the user equipment (UE) in an optimistic communication system scenario, where the base station (BS) is capable of generating several independent beams and also the UE is capable of using all of these.

Fig. 10 visualizes the NRP of the best BPR and the TNRP (sum of the NRP for all BPRs) for each RX position as a bar graph. For each measurement position six bars are given: A light blue, a dark blue, a light red, a dark red, a light yellow and a dark yellow bar. The light and dark bars overlap each other. The light blue bar corresponds to the TNRP with the TX placed at TX position 1 and the light red bar with the TX placed at TX position 2, respectively. The light yellow bar visualizes the sum of the light blue and light red bar, simulating the TNRP of the case where two TXs are transmitting simultaneously and all BPRs are used. This case simulates a MIMO scenario with macro-diversity. To give a more realistic approach on the topic of MIMO and macro-diversity, the NRP of the best BPR is also visualized as the darker graphs. The dark blue bar corresponds to the NRP of the best BPR with the TX placed at TX position 1 and the dark red bar with the TX placed at TX position 2, respectively. The dark yellow bar visualizes the sum of the dark blue and dark red bar, which corresponds to the sum of NRP for the two best BPRs. This simulates the case, where the UE can connect to two BSs each with one beam.

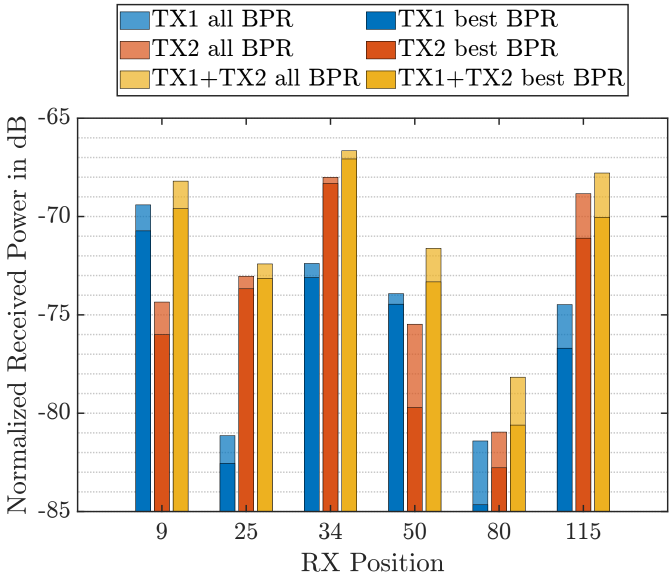

Figure 10: Bar plot visualizing the NRP for the best BPR (dark bars) and the TNRP - NRP of all BPRs - (light bars) for each RX position. The blue bars correspond to measurements with the TX placed at TX position one, and the red bars at TX position 2, respectively. The yellow bars visualizes the sum of the blue and red bar, simulating two simultaneously transmitting TXs.

Fig. 10 reports that the TNRP (light blue and light red bars) is always higher than the NRP of the best BPR (dark blue and dark red bars). This means, that for all measurements at least one additional BPR besides the best BPR is identified. The power difference ranges from 0.31 dB to 4.24 dB. The measurement with index 8 (RX position 50, TX position 2) benefits the most from the summation of residual BPRs with 4.24 dB. Since measurement 8 is a NLOS measurement, this implies that other scattered paths that may be used as potential BPRs have a NRP similar to the one of the best BPR. The average power difference between the TNRP and the NRP of the BPR for LOS measurements (measurement index 1, 2, 4, 5, 6, 7 and 12) is 1.12 dB. The average power difference for NLOS measurements (measurement index 3, 8, 9, 10 and 11) is 2.71 dB.

Another metric is determined which is the MDG. The MDG is given by the difference between the summed up and the individual received powers for each measurement. The MDG is separately determined for the optimistic and realistic adoption of a communication system. Explained in an illustrated manner, the MDG is the difference between the yellow bar to the red and blue respectively. For the realistic adoption of a communication system, the MDG is the difference between the dark yellow bar to the dark blue and red bar. For the the optimistic adoption of a communication system, the light bars respectively. Fig. 11 visualizes the MDGs for all measurements and all adaptions.

Fig. 11 reports that the MDG is strongly dependent on the measurement position and ranges from 0.53 dB to 9.41 dB. For RX position 9, 25, 34, 80 and 115 the MDG behaves similar for both TX positions for the best BPR and the all BPR case. The

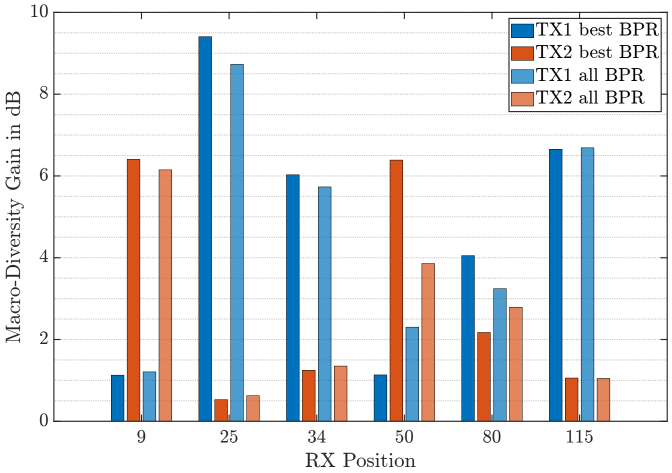

Figure 11: Bar plot visualizing the MDGs for the best BPR (dark bars) and all BPRs (light bars) for each RX and TX position.

obtained values are separated into LOS and NLOS dependent on the measurement as listed in Table 4 and described in Section 3. By calculating the mean values, the average MDG for LOS of 3.2 dB and for NLOS of 5.7 dB is obtained for this scenario.

This means, that from a sub-THz communication system point of view an additional TX at least doubles the expected received power at the RX. Especially for NLOS positions the received power is enhanced drastically. Nevertheless, the gain in received power is dependent on the position of the additional TX and also the MIMO capability of the TXs and RX.

So far the NRPs of the BPRs have been evaluated separately for the two TX positions and each RX position. In the following, the two TX positions are evaluated together for the 6 RX positions. This means, that the identified BPRs for both TX positions at a certain RX position are combined. This results in 6 sets of BPRs - each for one RX position - that vary in length and in their NRPs. The sets are sorted by strength, so that the BPR with the highest NRP is first. Out of these sets, up to 4 of the strongest BPRs of each set are evaluated to give a statement about the expected range of the NRP at each RX position. Fig. 12 shows a box chart of the NRP for each RX position. The box chart includes the minimum expected NRP, which means only one BPR is regarded, the maximum expected NRP, which means all four BPR are regarded and also the cases where 2 or 3 BPRs are used.

This evaluation considers a sub-THz communication system that enables multiple beams both on the TXs' side and the RX's. The RX is capable of using up to 4 beams in parallel and the TXs are able to serve the UE in parallel. This evaluation assumes the given deployment of TXs as before and analyzes the impact of MIMO capability of the sub-THz communication system. In addition, the system's resilience to blockage at the RX is analyzed. Fig. 12 gives a first impression on the NRP's behavior for all 6 RX positions if one to possible four BPRs are used within the system. Each box within the box chart is characterized by its minimum value, maximum value, lower quantile, upper quantile and the median. The upper dash corresponds to the maximum, the lower dash corresponds to the minimum, the box includes the quantiles and the dash within the box shows the median value.

Fig. 12 reports, that the minimum expected NRP for pure LOS measurement positions - RX position 9 and 34 - is the highest as expected. The figure also reports that the minimum expected NRP for the pure NLOS position - RX position 80 - is the lowest. All measurement positions benefit from the MDG and the MIMO capability assumption of the system. Measurement positions that are party LOS and NLOS, such as RX position 115, may reach up to the same maximum expected NRP as pure LOS positions. The difference between maximum and minimum expected NRP is in average smaller than 10 dB.

By discarding parts of the PAP, synthetic blockage is introduced to the system. When discarding a row of the PAP as visualized in Fig. 8 and Fig. 9, all AAoD for a specific AAoA are discarded. This simulates a single-directional blockage of the RX for one of the four AAoAs. When discarding more than one row, severe blockage of the RX from multiple directions is simulated.

Fig. 13 visualizes the NRP for all RX positions for a single-directional blocker at the RX. For this visualization, the sets of BPRs have been manipulated, such that all cases of single-directional AAoA blockage have been simulated. This means, that for each set each of the AAoDs for each AAoA have been discarded consecutively. Same as for Fig. 12, one to four BPRs have been analyzed. Fig. 13 reports that the maximum expected NRP when using 4 BPRs has not been effected drastically. On the other hand, the minimum expected NRP for all RX positions has been decreased for more than 5 dB.

When comparing the median values of the NRPs of Fig. 12 and Fig. 13, the values have only decreased slightly for the single-directional blockage case. This implies a resilience of the sub-THz communication system against single-directional blockage, when using two TXs and the described MIMO capability.

When increasing the blocked area around the RX to three zones - three discarded lines of the PAP - the blockage becomes more severe. By discarding three neighboring AAoAs, only one to two BPR for one RX position are identified. Similar as before, the sets of BPRs have been manipulated for the severe blockage case and a box chart has been created. Fig. 14 visualized the NRP for all RX positions with multi-directional blockage. The figure reports, that the maximum and minimum expected NRP for all RX positions has been decreased, as anticipated. At the same time, the median values of the NRPs for each RX position have been decreased significantly. The range between the lower and upper quantile has also increased, which means that a higher variance of the NRP is expected. By comparing Fig. 14 to Fig. 12, the maximum values of the NRP of the multi-directional blockage case are comparable to the minimum values of the non blockage case. This indicates that the sub-THz communication system, as realized and assumed in this work, copes with multi-directional blockage at the RX side by exploiting up to four beams, as good as the case where no blockage affects the RX that only uses one beams provided either by TX1 or TX2.

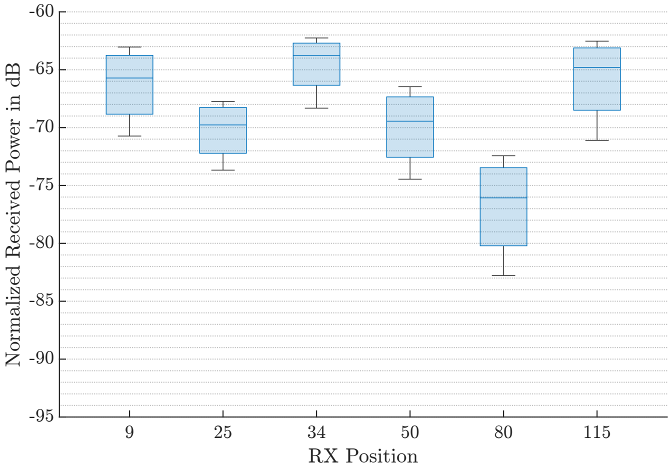

Figure 12: Box chart of the NRP for 1 to 4 BPRs used for each RX position.

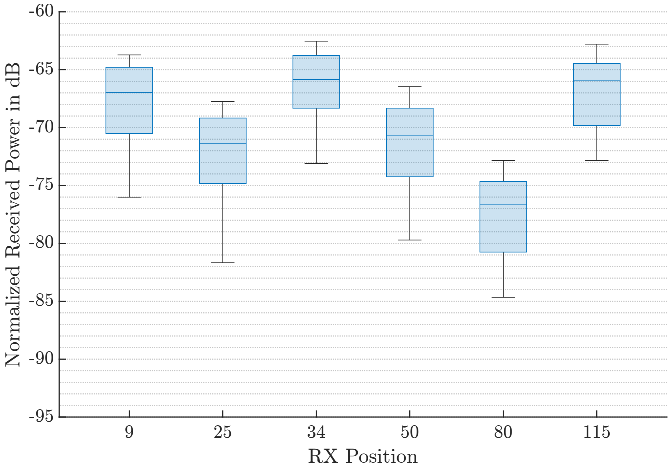

Figure 13: Box chart of the NRP for single-directional blockage.

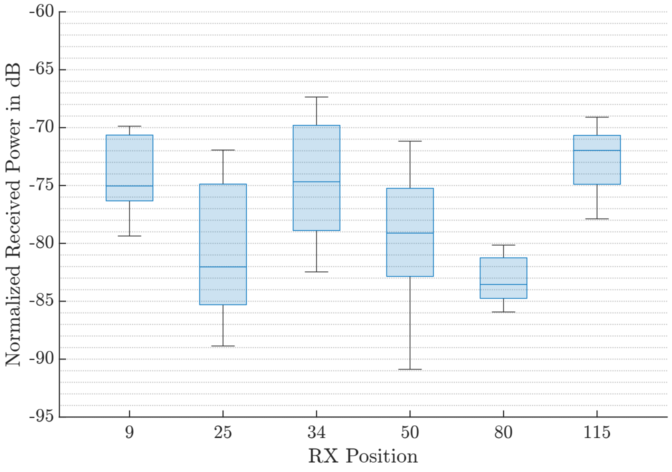

Figure 14: Box chart of the NRP with severe multi-directional blockage.

5. Conclusion

We performed a channel measurement campaign in a production hall of Rohde & Schwarz in Memmingen, Germany with a CS that operates in the D-band at a CF of 160 GHz. The channel measurement campaign targets the topics of beam-steering, MIMO, MDGs and blockage for sub-THz channels in industrial environments. Therefore, six RX and two TX positions were chosen at which measurements for all possible beam configurations were performed. The measurements cover all possible combinations of LOS and NLOS cases. By rotating both the TX and RX in the azimuth domain, an angular resolution of 15° for a range of −60° to 60° in the AAoD and a resolution of 90° for a range of 0° to 270° in the AAoA is obtained. By identifying independent BPRs in the PAP and summing up their NRPs, the MDGs are analyzed for single-input single-output (SISO) and MIMO channels. Our measurements report that for this explicit scenario, a MDG of 3.2 dB for LOS and 5.7 dB for NLOS is obtained. By discarding certain areas of the PAP, single-directional and multi-directional blockage and its impact on the expected received power have been analyzed. The results report that for single-directional blockage of the RX the NRP in average is not drastically effected, due to the two TX setup. Both the simulated MIMO capability and also macro-diversity counter the blockage effectively.

Acknowledgment

The authors acknowledge the financial support by the Federal Ministry for Research, Techonology and Space (BMFTR) in Germany in the programme of “Souverän. Digital. Vernetzt.” Joint project 6G-RIC, project identification number: 16KISK020K.

References

[1] *World Radiocommunication Conference 2023 (WRC-23) – Provisional Final Acts*, International Telecommunication Union (ITU) Std., Dec. 2023.

[2] “ETSI GR THz 001 - V1.1.1: TeraHertz modeling (THz); Identification of use cases for THz communication systems,” https://www.etsi.org/deliver, accessed on January 2024.

[3] “ETSI GR THz 002 - V1.1.1: TeraHertz technology (THz); Identification of frequency band of interest for THz communication systems,” https://www.etsi.org/deliver, accessed on January 2024.

[4] “ETSI GR THz 003 - V1.1.1: TeraHertz modeling (THz); Channel measurements and modeling in THz bands,” https://www.etsi.org/deliver, accessed on January 2024.

[5] “ETSI GR THz 004 - V1.1.1: TeraHertz technology (THz); RF hardware modeling,” https://www.etsi.org/deliver, accessed on January 2024.

[6] Y. Wang *et al.*, “Millimeter wave and sub-THz channel measurements, models and comparisons in indoor industrial environment,” in *2024 IEEE 99th Vehicular Technology Conference (VTC2024-Spring)*, 2024, pp. 1–5.

[7] S. Ju and T. S. Rappaport, “142 GHz multipath propagation measurements and path loss channel modeling in factory buildings,” in *ICC 2023 - IEEE International Conference on Communications*, 2023, pp. 5048–5053.

[8] S. Ju, *et al.*, “142 GHz sub-terahertz radio propagation measurements and channel characterization in factory buildings,” *IEEE Transactions on Wireless Communications*, vol. 23, no. 7, pp. 7127–7143, 2024.

[9] S. Ju and T. S. Rappaport, “Statistical channel model of wideband sub-thz radio propagation in indoor factories at 142 ghz: Towards 6g industrial wireless networks,” *IEEE Transactions on Wireless Communications*, pp. 1–1, 2024.

[10] A. Al-Jazri, J. Hu, and S. Salous, “Indoor measurements in industrial environment in the sub-thz band,” in *2024 4th URSI Atlantic Radio Science Meeting (AT-RASC)*, 2024, pp. 1–3.

[11] A. Schultze *et al.*, “Dual-polarized sub-THz channel measurements in D-band in an industrial environment,” in *2024 Joint European Conference on Networks and Communications & 6G Summit (EuCNC/6G Summit)*, 2024, pp. 582–586.

[12] A. Schultze, M. Schmieder, R. Askar, M. Peter, W. Keusgen, and T. Eichler, “Beam-steered sub-thz channel measurements in d-band in an industrial environment,” in *2025 19th European Conference on Antennas and Propagation (EuCAP)*, 2025, pp. 1–5.

[13] X. Liao *et al.*, “Measurement-based channel characterization in indoor IIoT scenarios at 220 GHz,” in *2024 IEEE Wireless Communications and Networking Conference (WCNC)*, 2024, pp. 1–6.

[14] A. Schultze *et al.*, “Angle-resolved THz channel measurements at 300 GHz in an industrial environment,” in *2022 IEEE 95th Vehicular Technology Conference: (VTC2022-Spring)*, 2022, pp. 1–7.

[15] J. M. Eckhardt, A. Schultze *et al.*, “Uniform analysis of multipath components from various scenarios with time-domain channel sounding at 300GHz,” *IEEE Open Journal of Antennas and Propagation*, vol. 4, pp. 446–460, 2023.

[16] D. Dupleich *et al.*, “Spatial/temporal characterization of propagation and blockage from measurements at sub-THz in industrial machines,” in *2023 17th European Conference on Antennas and Propagation (EuCAP)*, 2023, pp. 1–5.

[17] C. E. Reinhardt *et al.*, “Channel measurements in an industrial environment for access point-to-sensor communication at 300 GHz,” in *2024 15th German Microwave Conference (GeMiC)*, 2024, pp. 308–311.

[18] A. Ghosh and M. Kim, “Thz channel sounding and modeling techniques: An overview,” *IEEE Access*, vol. 11, pp. 17 823–17 856, 2023.

[19] Y. Lyu *et al.*, “Design and validation of the phase-compensated long-range sub-thz vna-based channel sounder," *IEEE Antennas and Wireless Propagation Letters*, vol. 20, no. 12, pp. 2461–2465, 2021.

[20] Y. Lyu, Z. Yuan, M. Li, A. W. Mbugua, P. Kyösti, and W. Fan, "Enabling long-range large-scale channel sounding at sub-thz bands: Virtual array and radio-over-fiber concepts," *IEEE Communications Magazine*, vol. 62, no. 2, pp. 16–22, 2024.

[21] M. Schmieder *et al.*, "Channel measurements and large scale parameter estimation in a production hall," in *2021 IEEE 94th Vehicular Technology Conference (VTC2021-Fall)*, 2021, pp. 1–5.

[22] S. Wittig, M. Peter, and W. Keusgen, "A reference model for channel sounder performance evaluation, validation and comparison," in *2022 16th European Conference on Antennas and Propagation (EuCAP)*, 2022, pp. 1–5.

[23] "IEEE standard for definitions of terms for antennas," *IEEE Std 145-2013 (Revision of IEEE Std 145-1993)*, pp. 1–50, 2014.

[24] D. Chu, "Polyphase codes with good periodic correlation properties (corresp.)," *IEEE Transactions on Information Theory*, vol. 18, no. 4, pp. 531–532, 1972.

[25] M. Peter *et al.*, "Characterization of mm-wave channel sounders up to w-band and validation of measurement results," in *2016 10th European Conference on Antennas and Propagation (EuCAP)*, 2016, pp. 1–5.

[26] S. Wittig *et al.*, "On the dynamic range of digital correlative time domain radio channel measurements," *arXiv preprint arXiv:2008.07805*, 2020.